

Comparison of space-time evolutions of hot/dense matter in $\sqrt{s_{NN}}=17$ and 130 GeV relativistic heavy ion collisions based on a hydrodynamical model

Kenji Morita,^{1,*} Shin Muroya,^{2,†} Chiho Nonaka,^{3,‡} and Tetsufumi Hirano^{4,§}

¹*Department of Physics, Waseda University, Tokyo 169-8555, Japan*

²*Tokuyama Women's College, Tokuyama, Yamaguchi 745-8511, Japan*

³*The Institute of Physical and Chemical Research (RIKEN), Wako, Saitama, 351-0198, Japan*

⁴*Physics Department, University of Tokyo, Tokyo 113-0033, Japan*

Based on a hydrodynamical model, we compare 130 GeV/A Au+Au collisions at RHIC and 17 GeV/A Pb+Pb collisions at SPS. The model well reproduces the single-particle distributions of both RHIC and SPS. The numerical solution indicates that huge amount of collision energy in RHIC is mainly used to produce a large extent of hot fluid rather than to make a high temperature matter; longitudinal extent of the hot fluid in RHIC is much larger than that of SPS and initial energy density of the fluid is only 5% higher than the one in SPS. The solution well describes the HBT radii at SPS energy but shows some deviations from the ones at RHIC.

PACS numbers: 24.10.Nz, 12.38.Mh, 25.75.Gz

I. INTRODUCTION

One of the main purposes of ultra-relativistic heavy ion collision experiments is to explore the property of the hot and dense matter [1]. Recently the new experiment has begun to work at BNL-RHIC of which higher collision energy than other experiments up to now provides us chances to produce a new state of matter, quark-gluon plasma (QGP) with distinct possibility. However, the complicated collision processes composed of multiparticle productions and many-body interactions make it difficult to understand the properties of the hot matter. Therefore, a simple dynamical description of the system as a basis for the deeper understanding is indispensable.

Relativistic hydrodynamical models are well-established phenomenological tools for describing high energy nucleus-nucleus collisions and subsequent multiparticle production [2, 3, 4, 5, 6, 7, 8].

*Electronic address: morita@hep.phys.waseda.ac.jp

†Electronic address: muroya@yukawa.kyoto-u.ac.jp

‡Electronic address: nonaka@rarfaxp.riken.go.jp

§Electronic address: hirano@nt.phys.s.u-tokyo.ac.jp

In this paper, we use a (3+1)-dimensional hydrodynamical model [9] with a QCD phase transition. We assume a cylindrical symmetry to the collision dynamics. Thus, our discussion is limited to the central collisions only. By virtue of the simple picture of our model, we can easily analyze both SPS and RHIC data with the same numerical code. Most of hydrodynamical calculations for RHIC data use Bjorken’s scaling solution [2] for the longitudinal direction. For example, Kolb *et al.* analyzed hadronic transverse mass spectra and anisotropic flow [10]. Zschesche *et al.* [11] investigated the HBT radii. These calculations assume the longitudinal boost-invariant infinite source. Though recently some hybrid models are used [12, 13, 14] for the description of the hadronic phase, we here use a conventional description in which the hadronic phase is in local equilibrium.

In this paper, concentrating our discussion on the central collisions, we reproduce the single-particle spectra of hadrons at the beginning. In the hydrodynamical model, single-particle distributions are used as inputs in order to determine initial parameters rather than outputs. However, it is not trivial whether we succeed to reproduce experiments with “natural parameters” or not. Based on the solutions of hydrodynamical equations, we discuss the physical properties and the space-time evolution of the fluids in SPS and RHIC. We also evaluate the two-pion correlation functions and analyze the HBT radii. As a subsequent work of Ref. [15], we focus our discussion on comparison of the RHIC results and the SPS results based on the same numerical code.

As is well-known, the two-particle correlation function gives us information on the size of the particle source [16, 17]. In the cases of the relativistic heavy ion collisions, the correlation function tells us about the freeze-out which should be far from the static source. Thus, dynamical models such as hydrodynamical models are indispensable for understanding the relation between observed correlation functions and the space-time history of the system. However, up to now, any dynamical model assuming QGP failed to explain the experimental HBT radii in RHIC consistently with the single-particle spectra [11, 18] and elliptic flow [19], as being known as “HBT puzzle”.¹ We study the HBT radii in the framework of a hydrodynamical model which takes account of both transverse and longitudinal flow appropriately with a simple initial condition.

In the next section, we explain our model. In Sec. III, we discuss the space-time evolution of the fluid. In Sec. IV, we present the result of two-particle correlation. Section V is devoted for the concluding remarks.

¹ In Ref. [20], a hadronic rescattering model is shown to reproduce these quantities.

II. HYDRODYNAMICAL MODEL

Let the system achieve the local thermal and chemical equilibrium shortly after a collision of two incident nuclei. This relaxation process cannot be described by the hydrodynamical model. The hydrodynamical model starts at initial time, τ_0 , at which thermal and chemical equilibrium are established at least locally. The hydrodynamical equations are given as

$$\partial_\mu T^{\mu\nu} = 0. \quad (1)$$

We assume the perfect fluid for simplicity. Hence, energy-momentum tensor is given as

$$T^{\mu\nu} = (\epsilon + P)U^\mu U^\nu - P g^{\mu\nu}, \quad (2)$$

with U^μ , ϵ and P being four velocities of a fluid element, energy density and pressure, respectively. These are treated as local quantities. We numerically solve the above equations together with the net baryon number conservation law,

$$\partial_\mu (n_B U^\mu) = 0, \quad (3)$$

where n_B is the net baryon number density and is also treated as a local quantity. Putting the z axis as a collision axis, we use a cylindrical coordinate system as follows;

$$t = \tau \cosh \eta, \quad (4)$$

$$x = r \cos \phi, \quad (5)$$

$$y = r \sin \phi, \quad (6)$$

$$z = \tau \sinh \eta. \quad (7)$$

Focusing our discussion on central collisions, we may assume the cylindrical symmetry on the system. Therefore, by virtue of an identity $U_\mu U^\mu = 1$, the four velocity can be expressed by two rapidity-like variables Y_L and Y_T ;

$$U^\tau = \cosh(Y_L - \eta) \cosh Y_T, \quad (8)$$

$$U^\eta = \sinh(Y_L - \eta) \cosh Y_T, \quad (9)$$

$$U^r = \sinh Y_T. \quad (10)$$

Most of hydrodynamical calculations which analyze RHIC data use Bjorken's scaling solution $Y_L = \eta$. Putting the solution as an ansatz reduces numerical tasks very much but the analyses are limited to midrapidity region only. We solve not only transverse expansion but also the longitudinal

expansion explicitly. Numerical procedure for solving the coupled equations (1) and (3) is explained in [9]. In this algorithm, we solve the entropy and baryon number conservation law explicitly. Throughout our calculation, the total energy, entropy and baryon number are conserved within 5% of accuracy at the time step $\delta\tau = 0.01$ fm/c.

In order to solve the hydrodynamical equations, we must fix the equation of state (EoS). We adopt a bag model EoS with a first order phase transition. The QGP phase is composed of a free gas of massless u, d, s quarks and gluons. Hadronic phase is also assumed to be a free gas but with excluded volume correction. All hadrons are included up to 2 GeV/ c^2 of mass except for hyperons. Putting the critical temperature as $T_c = 160$ MeV at vanishing baryon density, we get the bag constant $B^{1/4} = 233$ MeV. We display the pressure as a function of temperature and baryonic chemical potential in Fig. 1. See [21] for the further detail of the EoS and numerical treatment of the first order phase transition in solving the hydrodynamical equations.

We assume that the system achieves local equilibrium and begins to expand hydrodynamically at $\tau = \tau_0 = 1.0$ fm/c. We put the initial conditions on this hyperbola. Bjorken's scaling solution is used as the initial condition of the longitudinal flow. Transverse flow is simply neglected at the initial time. We parameterize the initial energy density distribution $\epsilon(\tau_0, \eta, r)$ and net baryon number density distribution $n_B(\tau_0, \eta, r)$ as,

$$\epsilon(\tau_0, \eta, r) = \epsilon_{\max} \exp \left[-\frac{(|\eta| - \eta_0)^2}{2 \cdot \sigma_\eta^2} \theta(|\eta| - \eta_0) - \frac{(r - r_0)^2}{2 \cdot \sigma_r^2} \theta(r - r_0) \right], \quad (11)$$

$$n_B(\tau_0, \eta, r) = n_{B0} \left\{ \exp \left[-\frac{(\eta - \eta_D)^2}{2 \cdot \sigma_D^2} \right] + \exp \left[-\frac{(\eta + \eta_D)^2}{2 \cdot \sigma_D^2} \right] \right\} \exp \left[-\frac{(r - r_0)^2}{2 \cdot \sigma_r^2} \theta(r - r_0) \right]. \quad (12)$$

The energy density distribution of the longitudinal direction (11) has a central plateau characterized by η_0 and a gaussian tail whose width is given by σ_η (Fig. 2), while the net baryon number distribution is a superposition of the two gaussians of which peaks exist at $\pm\eta_D$. For the transverse direction, both are parametrized by a flat region with gaussian smearing near the edge (Fig. 3). For a nucleus with mass number A , the relation among these quantities is given by $\sigma_r + r_0 = 1.2A^{1/3}$.² Once these parameters are fixed, we can solve the hydrodynamical equations and pursue the space-time evolution of the fluid. These initial parameters are so chosen that the model reproduces the single-particle spectra measured in the experiments. The single-particle spectra can be calculated by making use of the Cooper-Frye formula [22]

$$E_{\mathbf{k}} \frac{dN_i}{d^3\mathbf{k}} = \frac{g_i}{(2\pi)^3} \int_{\Sigma} k_\mu d\sigma^\mu \frac{1}{\exp[(U_\nu k^\nu - \mu_B)/T_f] \mp 1}, \quad (13)$$

² We adopt the initial condition as a natural and the simplest extension of the (1+1)-dimensional Bjorken's picture [2] and as a basis for the further improvement.

where g_i is a degeneracy of the hadrons and T_f is a freeze-out temperature. The sign is plus for fermions and minus for bosons. Integration is performed on 3-dimensional freeze-out hypersurface Σ . By virtue of the Lagrangian hydrodynamics, contribution from the time-like hypersurface is expected to be small and the space-like hypersurface dominates the particle emission at freeze-out; we employ the non-covariant prescription $k_\mu d\sigma^\mu \simeq k_\tau d\sigma^\tau$ for the sake of simplicity in the numerical treatment. In this approximation, total counted energy evaluated from Eq.(13) is slightly larger than 90% of the total energy of the initial fluid; we regard the approximation works well enough. At SPS, we assume that the freeze-out occurs at a energy density ϵ_f and at a temperature T_f , at the RHIC energy. We also assume that the thermal and the chemical freeze-out are taken to happen simultaneously. We show the freeze-out lines and the phase boundary on $T - \mu_B$ plane in Fig. 4. Note that two freeze-out lines in the figure do not differ at low baryonic chemical potential (Fig. 4).

We take account of the particles emitted from resonance decay as well as the direct emission from the freeze-out hypersurface. We include the decay processes $\rho \rightarrow 2\pi$, $\omega \rightarrow 3\pi$, $\eta \rightarrow 3\pi$, $K^* \rightarrow \pi K$, and $\Delta \rightarrow N\pi$ [23, 24]. These resonances are also assumed to be thermally emitted from the freeze-out hypersurface.

Two sets of initial parameter are summarized in Table I. Figures 5-7 show single-particle spectra in 17 AGeV Pb+Pb collisions at SPS. Our model well reproduces the experimental data with parameters in Table I. Also in 130 AGeV Au+Au collisions, our model shows good agreement with the data as in Figs. 8-11. However, we note that our model fails to produce enough number of anti-protons and overestimates the kaon yield in Fig. 10, where we multiply factors of 0.6 for kaons and 3.5 for anti-protons for clear comparison of the slopes [15]. This discrepancy may indicate the need for more sophisticated freeze-out mechanism.

III. SPACE-TIME EVOLUTION

In this section, we present the numerical solution of the hydrodynamical equations and discuss differences in the space-time evolutions of the fluids between RHIC and SPS. Figures 12 and 13 show space-time evolution of the fluid on the transverse plane. We also display the space-time evolution on the longitudinal plane in Fig. 14. Longitudinal flow and transverse flow are shown in Figs. 15 and 16, respectively. From Table I, the maximum energy density in RHIC is only 5% higher than the one in SPS. Only 5% higher energy density for the almost 50% larger dN/dY seems surprising result. We show the number density of the thermal negative pions emitted into midrapidity as a function of the space-time rapidity η of the freeze-out point (Fig. 17). This figure informs us

that thermal contribution of the volume element at $\eta = 0$ to the particles into midrapidity is only 9% larger in RHIC than in SPS. However, the wider region of the freeze-out hypersurface in η contributes to the midrapidity particle distribution in RHIC more than in SPS. As a result, factor 1.5 times larger number of particles obtained in the midrapidity region after summing up particles emitted at different η . The difference between RHIC and SPS in Fig. 17 originates in the longitudinal extent $\eta_0 + \sigma_\eta$ (see also Fig. 2) and is direct consequence of longitudinal dynamics. We also plot the entropy per unit flow rapidity dS/dY_L in Fig. 18. This is a conserved quantity if the boost-invariance is kept. In both RHIC and SPS, reflecting the deviation from the scaling solution shown in Fig. 15, entropy is shifted to the larger flow rapidity. Reduction of entropy at $Y_L = 0$, where $Y_L = \eta = 0$ always holds, comes from $dY_L/d\eta$ which is larger than unity [25]. Thus, the shift at RHIC is smaller than the one at SPS since the deviation from the boost-invariant solution is small (Fig. 15). At SPS, the difference of dS/dY_L between the initial stage and the final stage is larger than the case at RHIC.

Though our maximum energy density $6.0 \text{ GeV}/\text{fm}^3$ at initial is also so smaller than other calculation [10, 11, 26], this is due to the difference of initial time and transverse energy density profile of which nuclear thickness is considered. As for the average energy density at midrapidity, we get $\langle\epsilon_{\text{RHIC}}\rangle = 3.9 \text{ GeV}/\text{fm}^3$ and $\langle\epsilon_{\text{SPS}}\rangle = 3.77 \text{ GeV}/\text{fm}^3$. $\langle\epsilon_{\text{RHIC}}\rangle$ is a little smaller than an estimation of Ref. [27]. As a result of such a little difference in energy density, the space-time evolutions of two cases do not alter much in Figs. 12 and 13. The most different point is a longitudinal extension of the fluid, $\eta_0 + \sigma_\eta$. In RHIC, it is twice as large as in SPS. This is a consequence of much higher collision energy at RHIC. Indeed, the total energy of the fluid is 25290 GeV at RHIC, which is 99% of total collision energy. Hence, higher collision energy does not lead to higher energy density but is used to produce the matter with large volume at $\tau_0 = 1 \text{ fm}/c$.

The output from the fluids is summarized in Table II. Total net baryon number of the fluid is much smaller in RHIC than in SPS, as well as the mean chemical potential on the freeze-out hypersurface. This difference can be seen in the space-time evolution of temperature on $\eta - \tau$ plane (Fig. 14). As shown in Fig. 4, phase boundary can no longer be specified by temperature only but depends on both temperature and chemical potential in high net baryon density. For example, $T = 158 \text{ MeV}$ corresponds to the hadronic phase at vanishing baryon density. However, it can be in QGP phase at $\mu_B = 400 \text{ MeV}$ and be in mixed phase at some μ_B . This behavior is seen $T = 158 \text{ MeV}$ contour in Fig. 14, where the baryonic chemical potential becomes higher as η increases and a fluid element near $\eta \simeq 0.5$ stays at mixed phase for a long time. Such behavior does not appear in the RHIC case where chemical potential is small enough to characterize the mixed phase by the

almost constant temperature.

In Fig. 15 where deviation from Bjorken's scaling solution $Y_L - \eta$ is plotted, acceleration is larger in SPS than in RHIC because of the steeper pressure gradient of η -direction. Finally, the lifetime of each phase is also shown in Table II.

IV. TWO-PARTICLE CORRELATION

In this section, we present the result of the two-pion correlation function and HBT radii based on the numerical solution of the relativistic hydrodynamical equation. For simplicity, we assume that all the pions are emitted from a chaotic source and neglect the resonance contribution. Then, the two-particle correlation function is easily calculated through

$$C_2(q^\mu, K^\mu) = 1 + \frac{|I(q^\mu, K^\mu)|^2}{I(0, k_1^\mu)I(0, k_2^\mu)}, \quad (14)$$

where $K^\mu = (k_1^\mu + k_2^\mu)/2$, $q^\mu = k_1^\mu - k_2^\mu$, respectively [28, 29]. Here k_i^μ is *on-shell* momentum of i -th pion. We put

$$I(q^\mu, K^\mu) = \int K_\tau d\sigma^\tau(x) \sqrt{f(k_1, x)f(k_2, x)} e^{iq_\nu x^\nu}, \quad (15)$$

so that $I(0, k^\mu)$ reduces to the Cooper-Frye formula with $f(k, x)$ being the Bose-Einstein distribution function. Considering the experimental momentum acceptance, we integrate the correlation function with respect to the average momentum in region Ω as

$$C_2(q^\mu)|_\Omega = 1 + \frac{\int_\Omega K_T dK_T dY |I(q^\mu, K^\mu)|^2}{\int_\Omega K_T dK_T dY I(0, k_1^\mu)I(0, k_2^\mu)}. \quad (16)$$

The HBT radii are obtained by fitting the calculated correlation function (16) to gaussian fitting function

$$C_{2\text{fit}}(q^\mu) = 1 + \exp(-R_{\text{side}}^2 q_{\text{side}}^2 - R_{\text{out}}^2 q_{\text{out}}^2 - R_{\text{long}}^2 q_{\text{long}}^2 - R_{\text{ol}}^2 q_{\text{out}} q_{\text{long}}). \quad (17)$$

For RHIC data, in which rapidity acceptance $|Y| \leq 0.5$, the out-long cross term R_{ol} [30] can be ignored. According to the azimuthal symmetry, we can put $K_T = K_x$, $q_{\text{side}} = q_y$ and $q_{\text{out}} = q_x$.

Results of K_T dependence of the HBT radii are presented in Fig. 19 and 20, where we show the transverse momentum dependence HBT radii of the SPS Pb+Pb collisions and $M_T \equiv \sqrt{K_T^2 + m_\pi^2}$ dependence of the RHIC Au+Au collisions, respectively. In addition to the three radius parameters, we also present the ratio of R_{out} to R_{side} for better comparison between two collisions [31].

Sideward HBT radii (upper figures in Figs. 19 and 20) are consistent with the experiments in both RHIC and SPS. Larger radii than other calculations come from initial large transverse size of

the fluid. Outward HBT radii show quantitative agreement for the SPS data. However, qualitative behavior shows some deviation from the experimental data; our result takes the maximum value at $K_T \simeq 0.3$ GeV/ c while the experiment data seem to monotonically decrease except for the highest K_T bin. For the RHIC data, experimental data show steep decrease with M_T . On the other hand, our results are similar to the ones of SPS because of the similarity in the space-time evolution of both fluids. As for the longitudinal HBT radii, our model reproduces the qualitative behavior of the results of both experiments but shows a little overestimate at low M_T of RHIC result. Our result suggests that the longitudinal finite size effect is essential for understanding the behavior of R_{long} even at RHIC because other calculations assuming infinite boost invariant source show larger R_{long} [11, 19]. HBT radius in the longitudinal direction has two kinds of origin; spatial extent of the fluid [30] and thermal suppression caused by rapid expansion. The emission region is roughly characterized by a product of the Boltzmann factor $\exp[-m_T \cosh(Y_L - Y)/T]$ and a geometrical factor (e.g., $\exp(-\eta^2/2(\Delta\eta)^2)$). The deviation from the scaling solution causes stronger thermal suppression. As a result, our solution provides smaller longitudinal HBT radius. Our $R_{\text{out}}/R_{\text{side}}$ moderately increases with K_T in both SPS and RHIC. This tendency is also seen in a hybrid calculation [18] in spite of the quite different description of the hadronic phase. Our results show very good agreement with the SPS result, while the RHIC data clearly shows different behavior. As concerns the behaviors of R_{out} and $R_{\text{out}}/R_{\text{side}}$, opaque source [32] is a possible explanation if the current formalism of the two-particle correlation is correct. Though the opaque property appears in the hydrodynamical model by virtue of transverse flow [33], it is still insufficient to reproduce the small R_{out} in the RHIC experiment. More theoretical investigation will be required for solving the problem [20, 34].

Figure 21 shows the correlation functions projected onto each components of relative momenta. Transverse momentum of emitted pair is $0.125 \leq K_T \leq 0.225$ GeV/ c , which corresponds to the lowest momentum bin in Fig. 20. In each figure, calculated correlation functions are corrected by a common factor as $\lambda = 0.6$. The other kind of the reduction of the correlation function at $q_i = 0$ ($i = \text{side, out, long}$) is caused by an integration with respect to other components of the relative momenta. The resultant factor is in proportional to $1/R_i$. Our correlation function seems to be consistent with the experimental data for the outward and the longitudinal direction in spite of the overestimation of the HBT radii. Because the HBT radii correspond to the inverse width of the correlation function, difference in width between $R = 7$ fm and $R = 6$ fm is only about 5 MeV in relative momentum. The small value of sideward correlation function at $q_{\text{side}} = 0$ indicates that outward and longitudinal HBT radii are larger than the experimental results.

V. CONCLUDING REMARKS

In this paper, we investigate single-particle distributions and two-particle correlation functions in SPS Pb+Pb 17 AGeV collisions and RHIC Au+Au 130 AGeV collisions based on a hydrodynamical model in which both longitudinal and transverse expansion are taken into account. As long as the single-particle spectra, the hydrodynamical model well describes both SPS and RHIC data. The initial parameter set in the model for both collisions indicates that initial energy density in RHIC is only slightly higher than the one in SPS and much larger extent of hot matter is produced in RHIC, if we compare them at the same initial time and by similar initialization (Fig. 3 and Eqs. (11),(12)). We have also discussed the space-time evolution of the fluids. Since the initial conditions are not different so much, temperature and transverse flow evolution do not show significant difference between SPS and RHIC. Only the equi-temperature contour of $T = 158$ MeV shows the qualitative difference between SPS and RHIC due to the difference in net baryon number. Steeper pressure gradient in the longitudinal direction at SPS makes the deviation from the scaling solution larger than at RHIC. Two-pion correlation functions and the HBT radii are also investigated. Our model shows good agreement with the SPS data. For RHIC data, however, the outward and longitudinal HBT radii of our result are larger than the experimental data even though the dynamical longitudinal expansion and finite size effect are incorporated.

Acknowledgments

The authors would like to thank Prof. I. Ohba and Prof. H. Nakazato for their fruitful discussions and comments. They also would like to acknowledge J. Alam, R.S. Bhalerao, P. Kolb, L. McLerran, H. Nakamura, and F. Retière for valuable discussions and comments. This work was in part supported by the Ministry of Education, Science and Culture, Japan (Grant No. 11440080 and 13135221), Waseda University Grant for Special Research Projects No.2001A-888, Waseda University Media Network Center and ERI of Tokuyama University.

-
- [1] *Quark Matter 2001, Proceedings of the 15th International Conference on Ultra-Relativistic Heavy Ion Collisions* (North-Holland, 2002), edited by T. J. Hallman, D. E. Kharzeev, J. T. Mitchell and T. Ullrich. [Nucl. Phys. **A698**, 1c (2002)].
- [2] J. D. Bjorken, Phys. Rev. D **27**, 140 (1983).

- [3] H. von Gersdorff, L. McLerran, M. Kataja, and P. V. Ruuskanen, Phys. Rev. D **34**, 794 (1986); M. Kataja, P. V. Ruuskanen, L. McLerran, and H. von Gersdorff, *ibid.* **34**, 2755 (1986).
- [4] Y. Akase, M. Mizutani, S. Muroya, and M. Yasuda, Prog. Theor. Phys. **85**, 305 (1991); S. Muroya, H. Nakamura, and M. Namiki, Prog. Theor. Phys. Suppl **120**, 209 (1995).
- [5] J. Alam, S. Raha, and B. Sinha, Phys. Rep. **273**, 243 (1996).
- [6] U. Ornik, M. Plümer, B. R. Schlei, D. Strottman, and R. M. Weiner, Phys. Rev. C **54**, 1381 (1996).
- [7] C. M. Hung and E. V. Shuryak, Phys. Rev. C **57**, 1891 (1998).
- [8] P. F. Kolb, J. Sollfrank, and U. Heinz, Phys. Rev. C **62**, 054909 (2000).
- [9] T. Ishii and S. Muroya, Phys. Rev. D **46**, 5156 (1992).
- [10] P. F. Kolb, P. Huovinen, U. Heinz, and H. Heiselberg, Phys. Lett. B **500**, 232 (2001).
- [11] D. Zschesche, S. Schramm, H. Stöcker, and W. Greiner, Phys. Rev. C **65**, 064902 (2002).
- [12] S. A. Bass and A. Dumitru, Phys. Rev. C **61**, 064909 (2000).
- [13] D. Teaney, J. Lauret, and E. V. Shuryak, Phys. Rev. Lett. **86**, 4783 (2001).
- [14] D. Teaney, J. Lauret, and E. V. Shuryak, nucl-th/0110037.
- [15] T. Hirano, K. Morita, S. Muroya, and C. Nonaka, Phys. Rev. C **65**, 061902(R) (2002).
- [16] U. A. Wiedemann and U. Heinz, Phys. Rep. **319**, 145 (1999).
- [17] R. M. Weiner, Phys. Rep. **327**, 249 (2000).
- [18] S. Soff, S. A. Bass, and A. Dumitru, Phys. Rev. Lett. **86**, 3981 (2001); S. Soff, S. A. Bass, D. H. Hardtke, and S. Y. Panitkin, Phys. Rev. Lett. **88**, 072301 (2002).
- [19] U. Heinz and P. Kolb, hep-ph/0111075.
- [20] T. Humanic, nucl-th/0203004.
- [21] C. Nonaka, E. Honda, and S. Muroya, Eur. Phys. J. C **17**, 663 (2000).
- [22] F. Cooper and G. Frye, Phys. Rev. D **10**, 186 (1974).
- [23] J. Sollfrank, P. Koch, and U. Heinz, Z. Phys. C **52**, 593 (1991).
- [24] T. Hirano, Phys. Rev. Lett. **86**, 2754 (2001).
- [25] K. J. Eskola, K. Kajantie, and P. V. Ruuskanen, Eur. Phys. J. C **1**, 627 (1998).
- [26] T. Hirano, Phys. Rev. C **65**, 011901(R) (2002).
- [27] K. Adcox et al. (PHENIX Collaboration), Phys. Rev. Lett. **87**, 052301 (2001).
- [28] E. V. Shuryak, Phys. Lett **44B**, 387 (1973).
- [29] Y. Hama and S. S. Padula, Phys. Rev. D **37**, 3237 (1988).
- [30] S. Chapman, P. Scotto, and U. Heinz, Phys. Rev. Lett. **74**, 4400 (1995); S. Chapman, J. R. Nix, and U. Heinz, Phys. Rev. C **52**, 2694 (1995).
- [31] D. H. Rischke and M. Gyulassy, Nucl. Phys. **A608**, 479 (1996).
- [32] H. Heiselberg and A. P. Vischer, Eur. Phys. J. C **1**, 593 (1998).
- [33] K. Morita, S. Muroya, H. Nakamura, and C. Nonaka, Phys. Rev. C **61**, 034904 (2000). In this paper, we used a simpler hydrodynamical model than the present paper; we did not take account of baryon number nor particle productions through the resonances. EoS is also different.

- [34] L. McLerran and S. S. Padula, nucl-th/0205028.
- [35] H. Appelshäuser et al. (NA49 Collaboration), Phys. Rev. Lett. **82**, 2471 (1999).
- [36] A. Wuosmaa et al. (PHOBOS Collaboration), Nucl. Phys. **A698**, 88 (2002).
- [37] C. Adler et al. (STAR Collaboration), Phys. Rev. Lett. **87**, 112303 (2001).
- [38] J. Velkovska et al. (PHENIX Collaboration), to be published in the proceedings for International Conference on Physics and Astrophysics of Quark-Gluon Plasma (ICPAQGP-2001).
- [39] I. G. Bearden et al. (BRAHMS Collaboration), Phys. Rev. Lett. **87**, 112305 (2001).
- [40] C. Blume et al. (NA49 Collaboration), Nucl. Phys. **A698**, 104c (2002).
- [41] C. Adler et al. (STAR Collaboration), Phys. Rev. Lett. **87**, 082301 (2001).

Figures

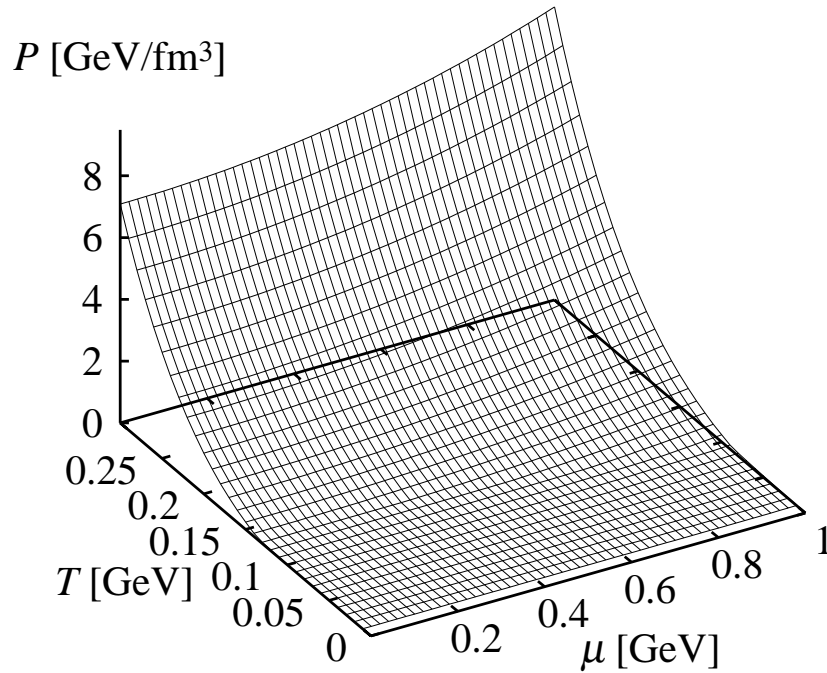


FIG. 1: Pressure $P(T, \mu_B)$ distribution

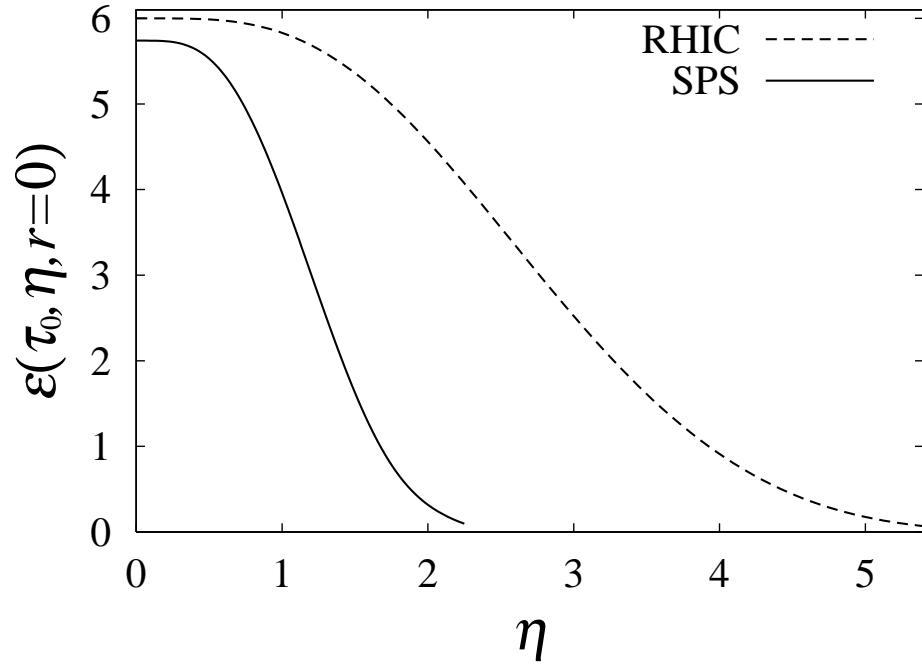
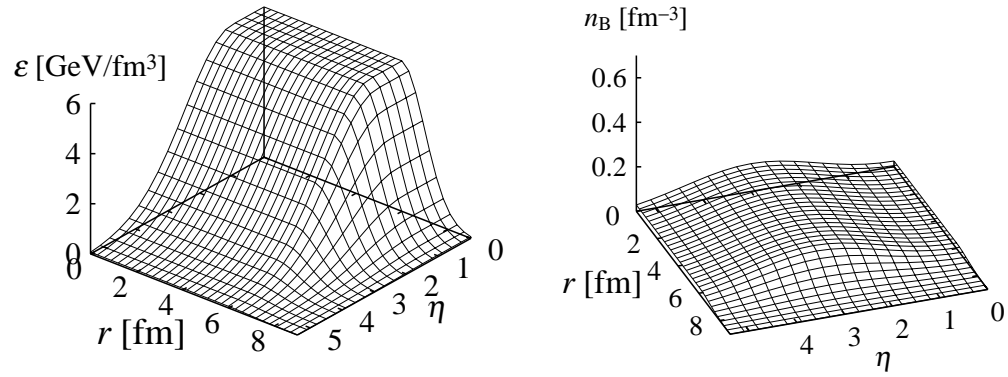


FIG. 2: Initial energy density distribution at $r = 0$ in η -direction. Dashed line stands for the RHIC case while solid line stands for the SPS case.

for RHIC 130A GeV Au+Au



for SPS 17A GeV Pb+Pb

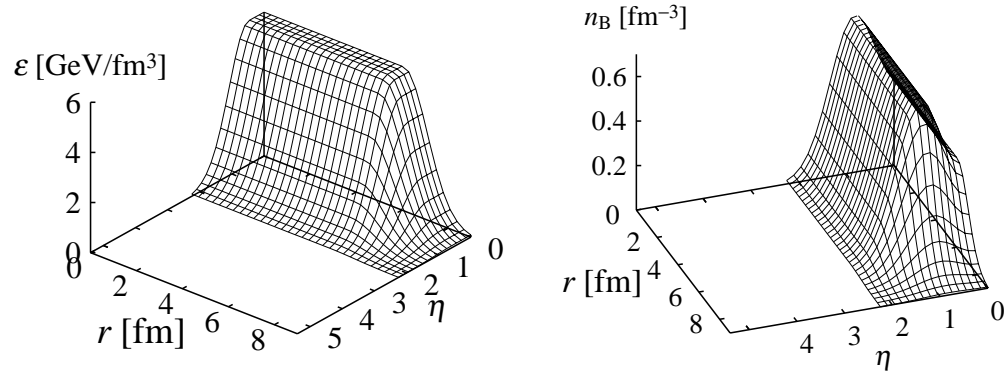


FIG. 3: Initial energy density (left) and net baryon number density (right) distribution for RHIC and SPS.

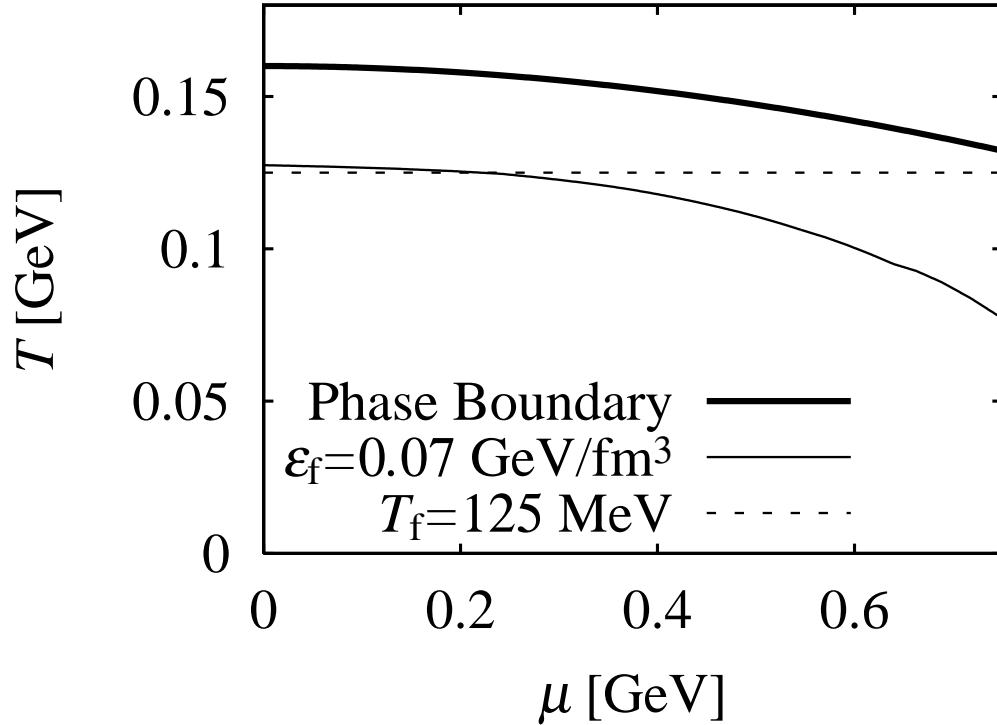


FIG. 4: Phase boundary (thick line) and freeze-out lines on $T-\mu_B$ plane. Thin solid line denotes the constant energy density contour as a freeze-out condition in SPS. Dashed line stands for constant temperature line, which is a freeze-out condition in RHIC.

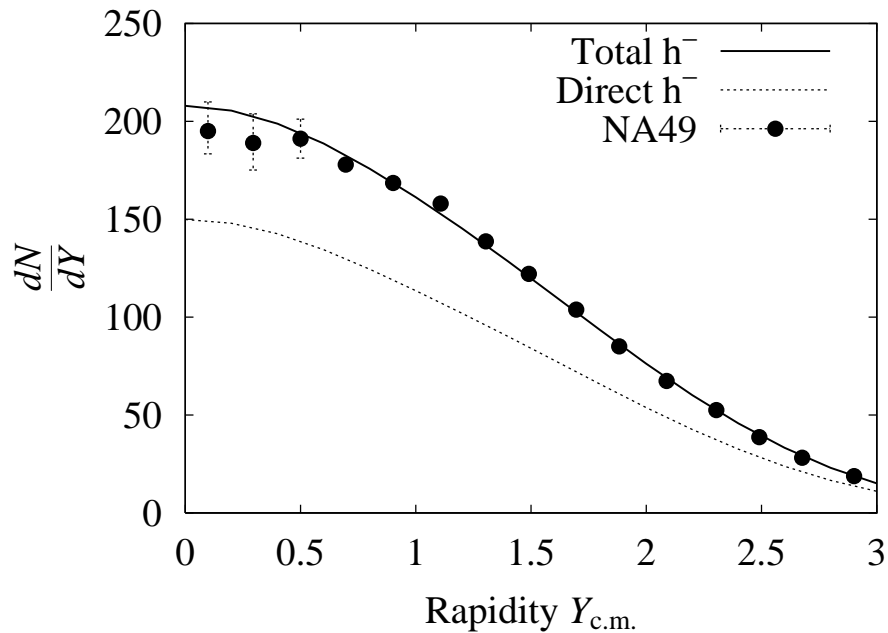


FIG. 5: Rapidity distribution of negatively charged hadrons in Pb+Pb collisions at SPS. Closed circles are experimental data which are taken from [35]. Solid and dashed lines stand for our result of total yield and contribution from direct particles.

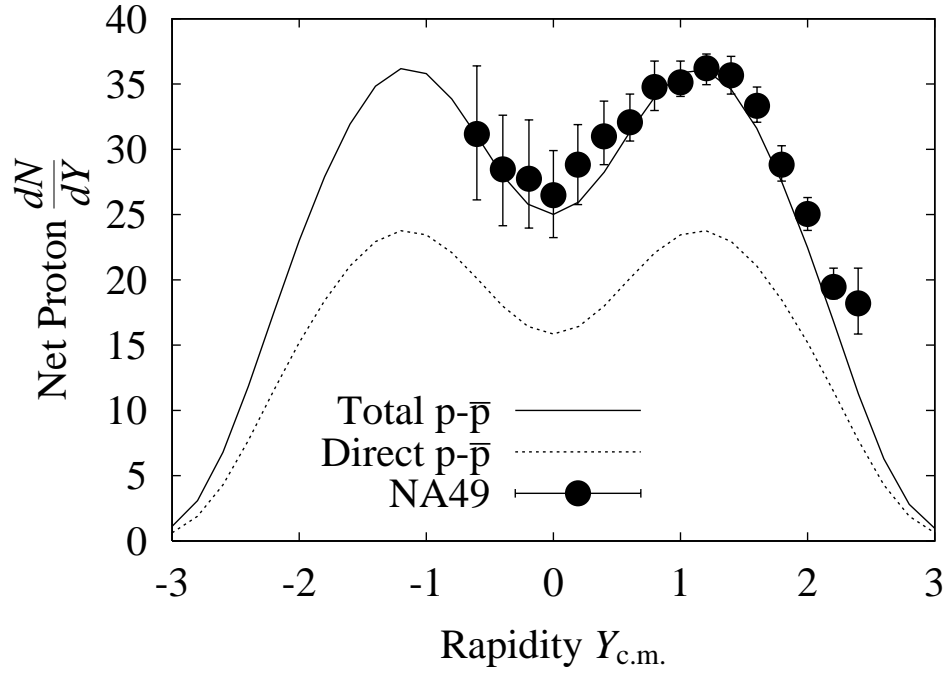


FIG. 6: Rapidity distribution of net protons in Pb+Pb collisions at SPS. Meanings of symbols and lines are the same as in Fig. 5.

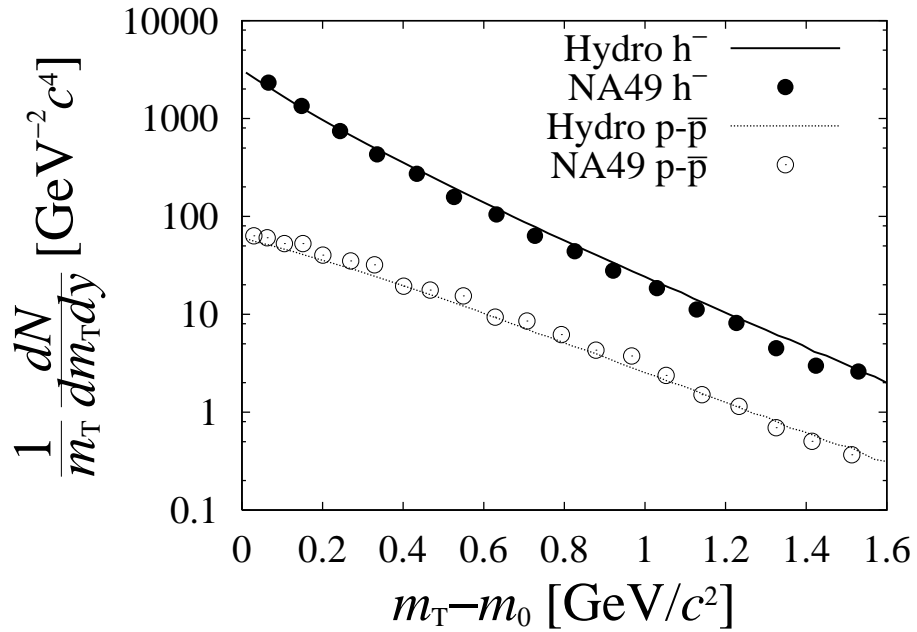


FIG. 7: Transverse mass distributions of negatively charged hadrons and net protons in Pb+Pb collisions at SPS. Closed and open circles are the experimental data of negatively charged hadrons and net protons, respectively. Solid and dashed lines stand for charged hadrons and net protons of our result, respectively.

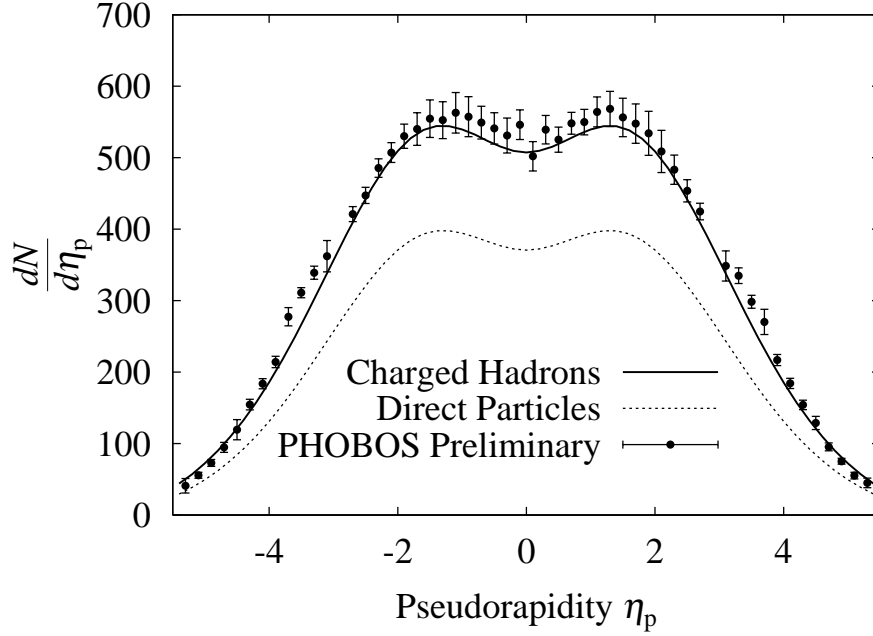


FIG. 8: Pseudorapidity η_p distribution of charged hadrons. Solid line shows our result (π, K, p) including resonance contribution. Dotted line denotes contribution of the directly emitted particles from the freeze-out hypersurface. Closed circles are preliminary result from the PHOBOS Collaboration [36].

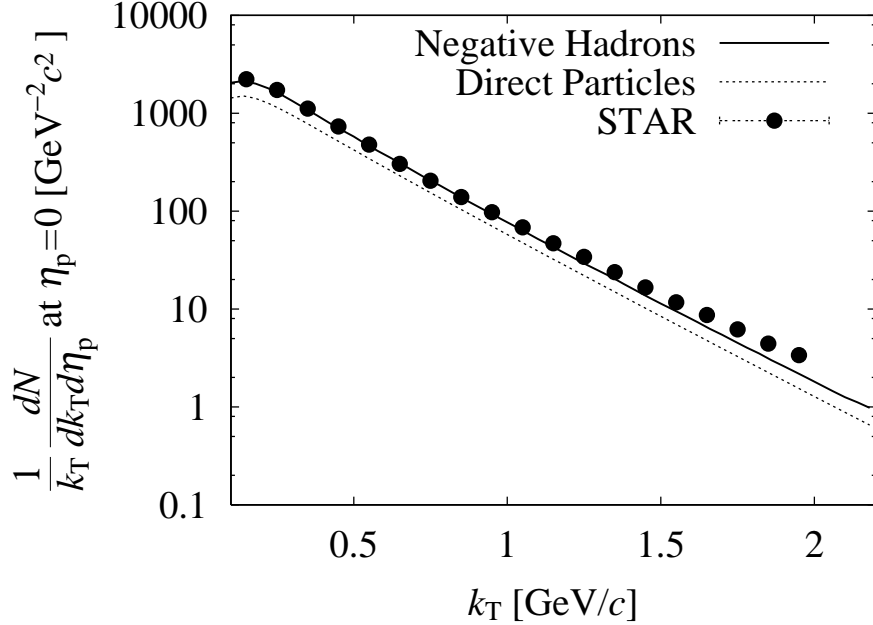


FIG. 9: Transverse momentum spectrum of negatively charged hadrons. As in Fig. 8, solid line and dotted line show total number of particles and directly emitted particles from the freeze-out hypersurface, respectively. Closed circles are data from the STAR Collaboration [37].

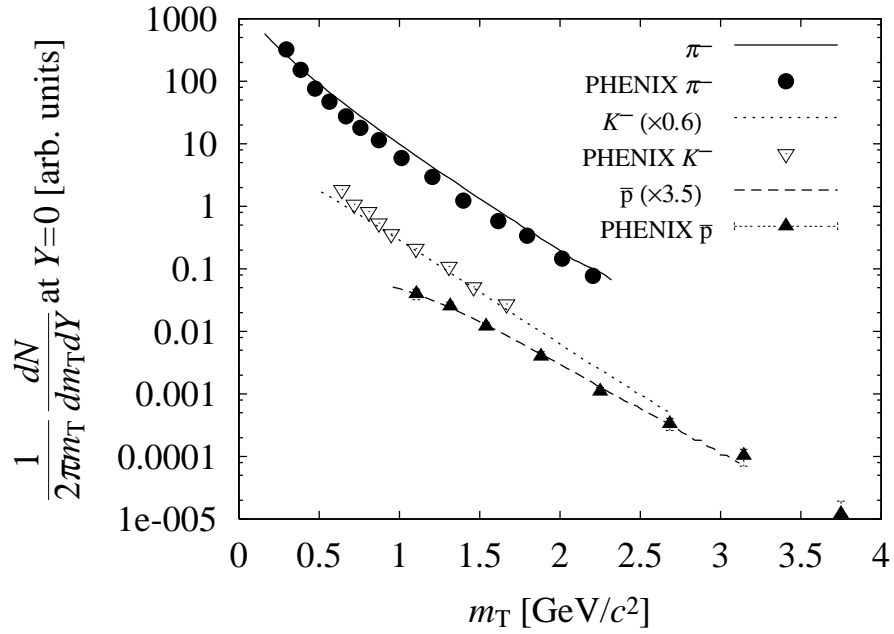


FIG. 10: Transverse mass spectra of negatively charged hadrons. Solid line, dotted line and dashed line denote π^- , K^- and \bar{p} yield of our result. K^- and \bar{p} spectra are scaled down by factor 0.1 and 0.01, respectively. Closed circles, open triangles and closed triangles are preliminary data from the PHENIX Collaboration [38].

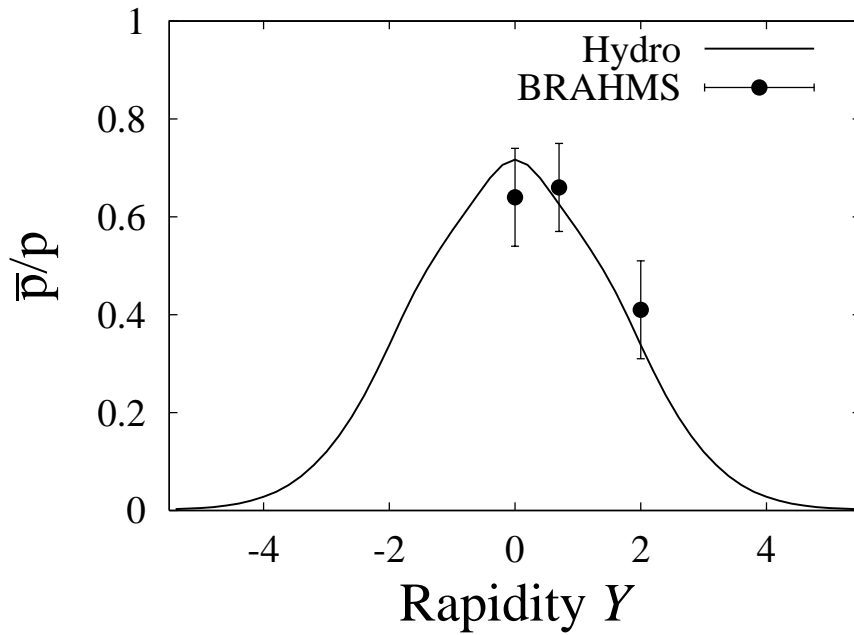


FIG. 11: Rapidity dependence of anti-proton to proton ratio. Experimental data are taken from the BRAHMS Collaboration [39].

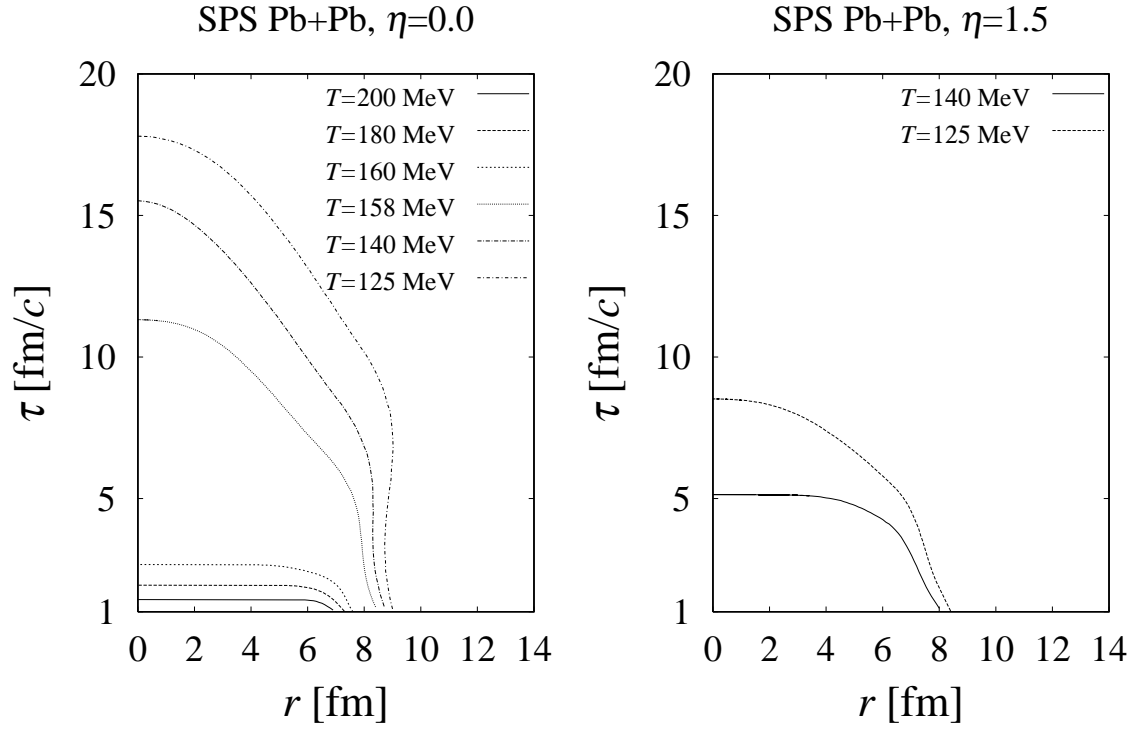


FIG. 12: Temperature contour on $r - \tau$ plane at SPS. Left: $\eta = 0$ section. Right: $\eta = 1.5$ section.

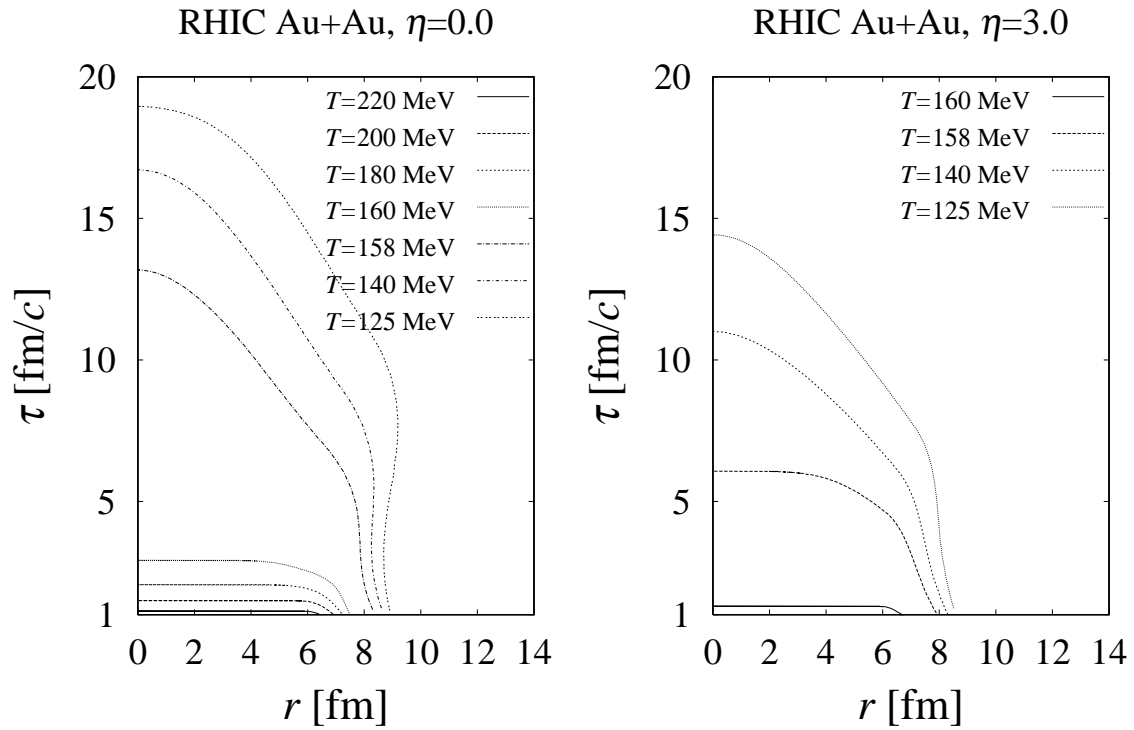


FIG. 13: Temperature contour on $r - \tau$ plane at RHIC. Left: $\eta = 0$ section. Right: $\eta = 3.0$ section.

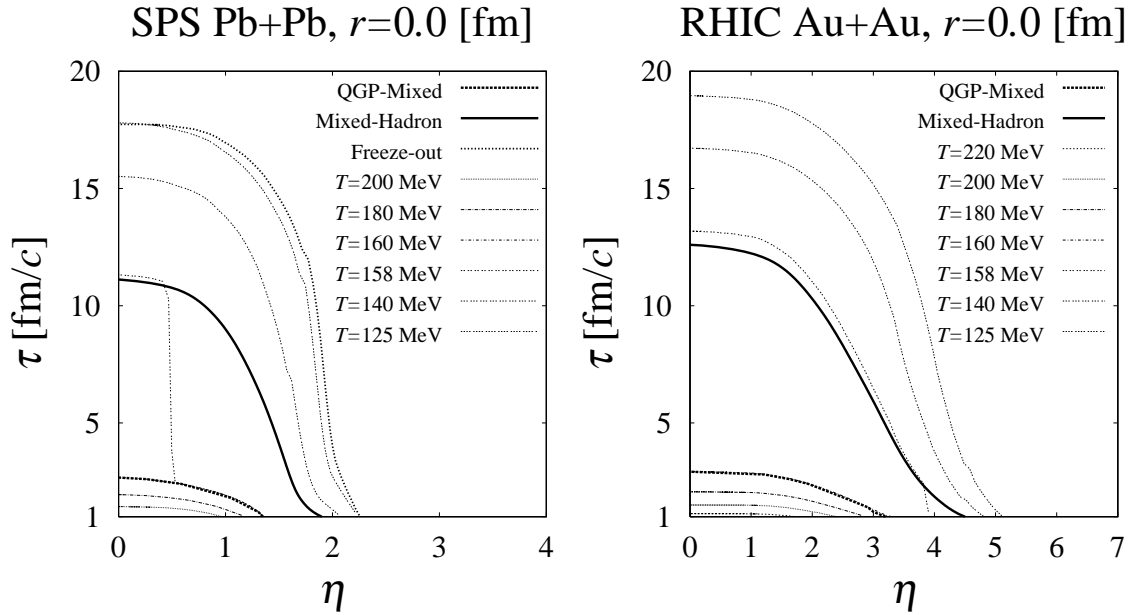


FIG. 14: Temperature contour on $\eta - \tau$ plane at $r = 0$ fm. Left figure shows the SPS case and right figure shows the RHIC case. Thick solid (dashed) line shows the phase boundary between mixed (QGP) phase and hadronic (mixed) phase. Freeze-out line is given as dotted line for the SPS. As for RHIC, $T_f = 125$ MeV contour corresponds to the freeze-out line.

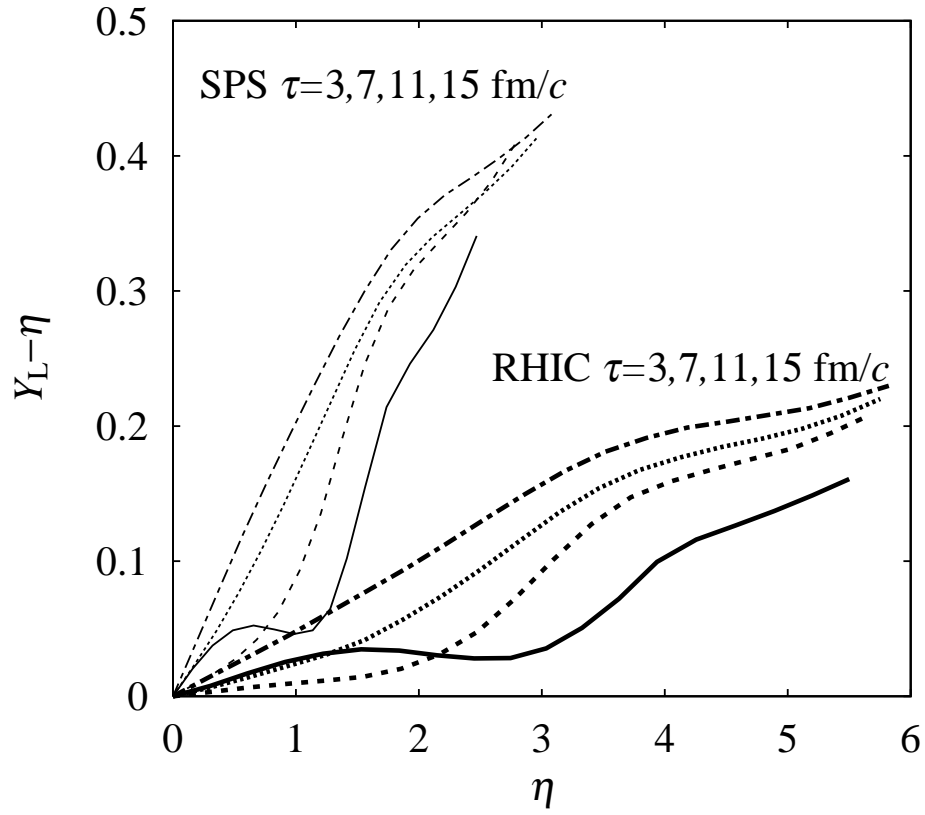


FIG. 15: Space-time evolution of longitudinal flow at $r = 0$. Deviation from Bjorken's scaling solution of longitudinal flow rapidity is plotted. Thick lines stand for the RHIC case and thin lines stand for the SPS case. In both cases, solid lines, dashed lines, dotted lines and dash-dotted lines denote $\tau = 3, 7, 11$ and 15 fm/c cases, respectively.

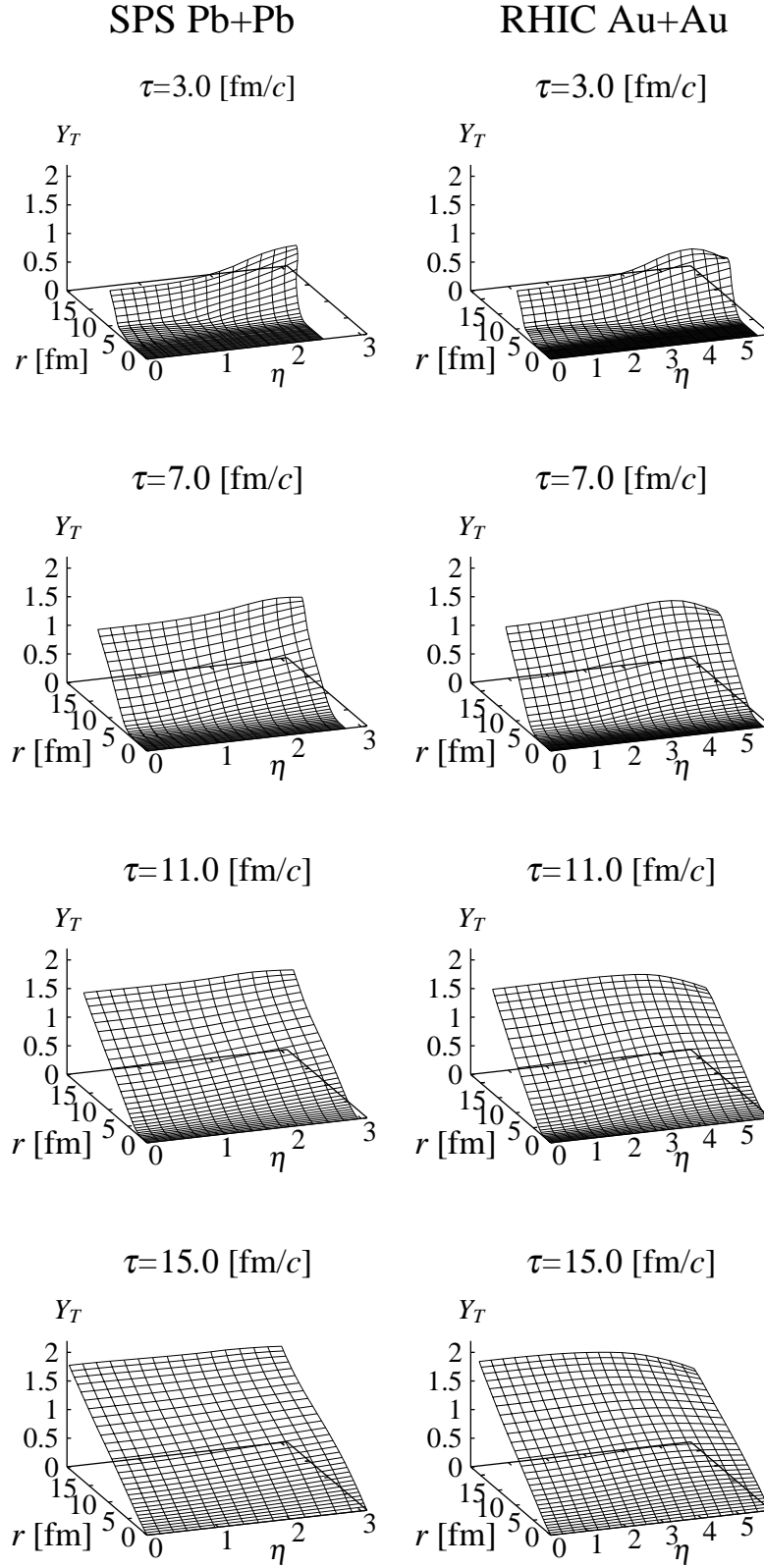


FIG. 16: Space-time evolution of transverse flow. Left and right column show the SPS and the RHIC cases, respectively.

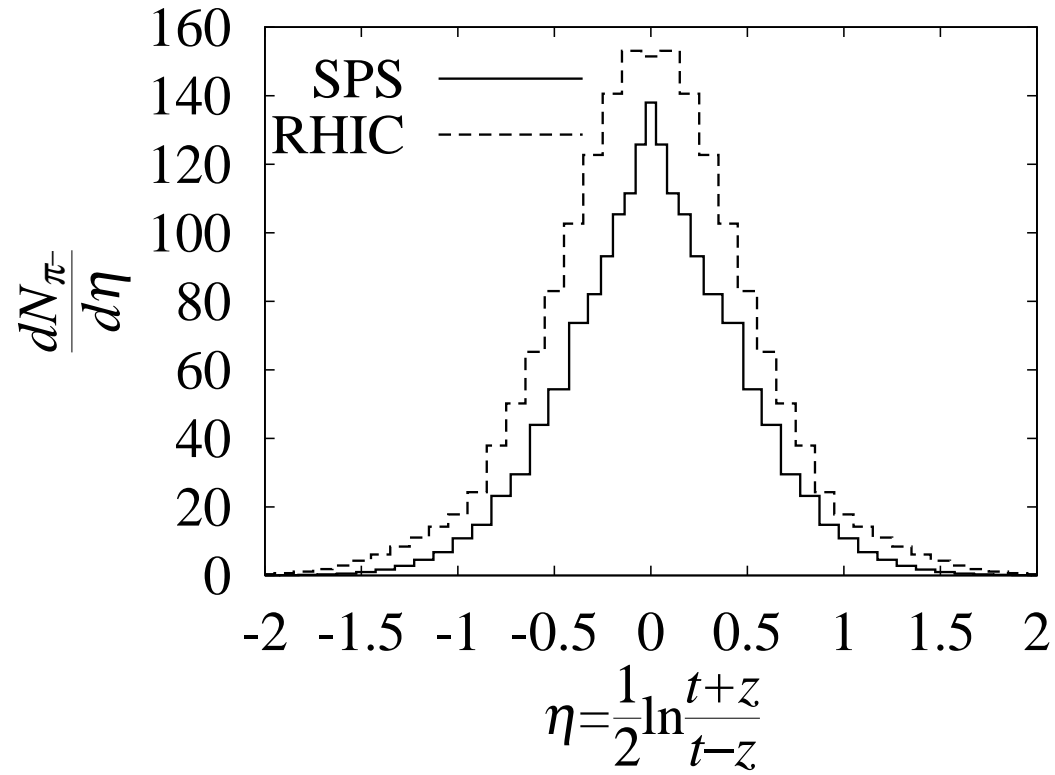


FIG. 17: Number density of the particles emitted into the midrapidity region as a function of space-time rapidity of the source point. Solid line stands for the SPS case and dashed line stands for the RHIC case.

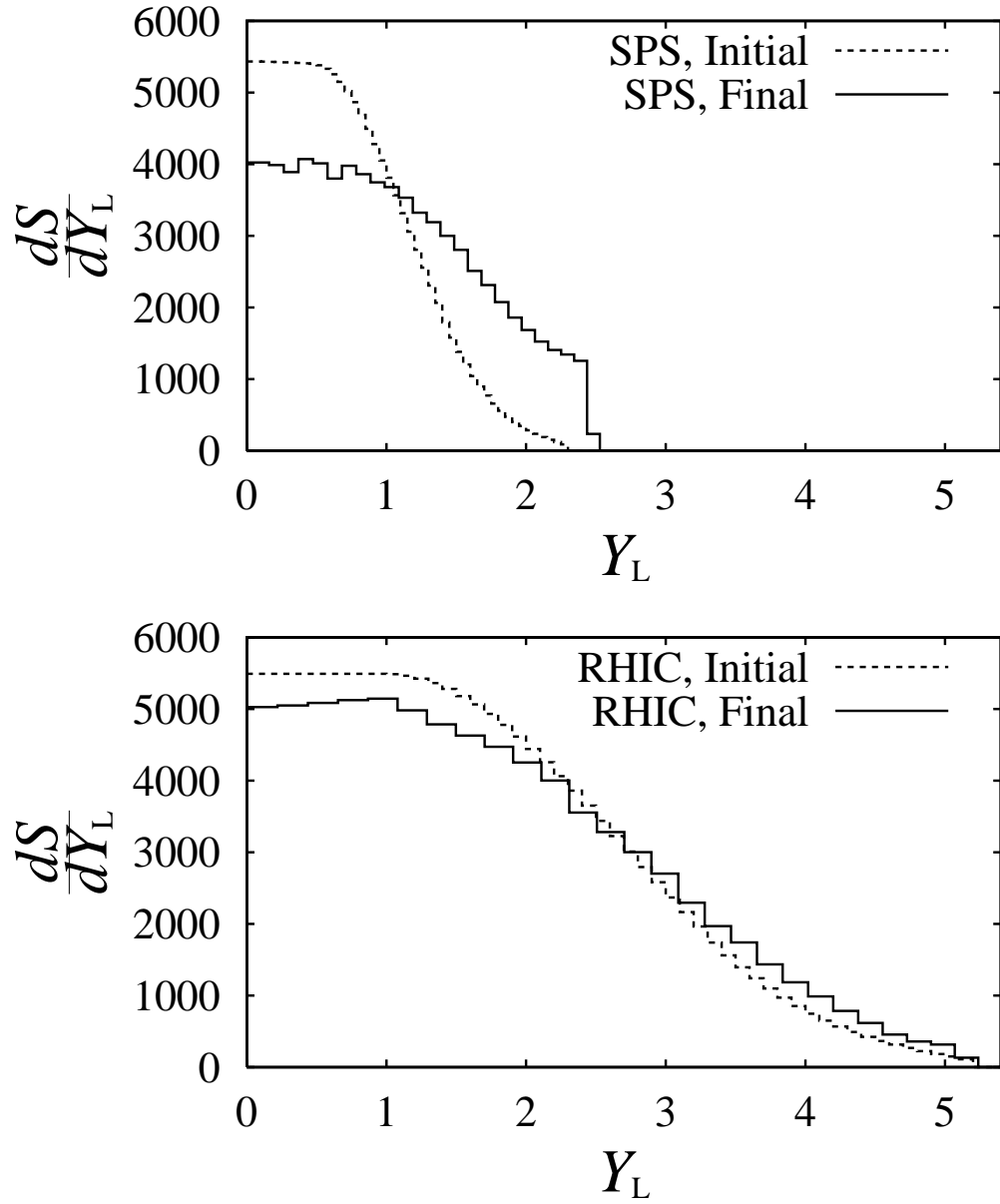


FIG. 18: Entropy per unit flow rapidity. In both figures (upper for SPS and lower for RHIC), solid lines stand for the quantities calculated on the freeze-out hypersurface and dashed lines stand for the one on the initial stage.

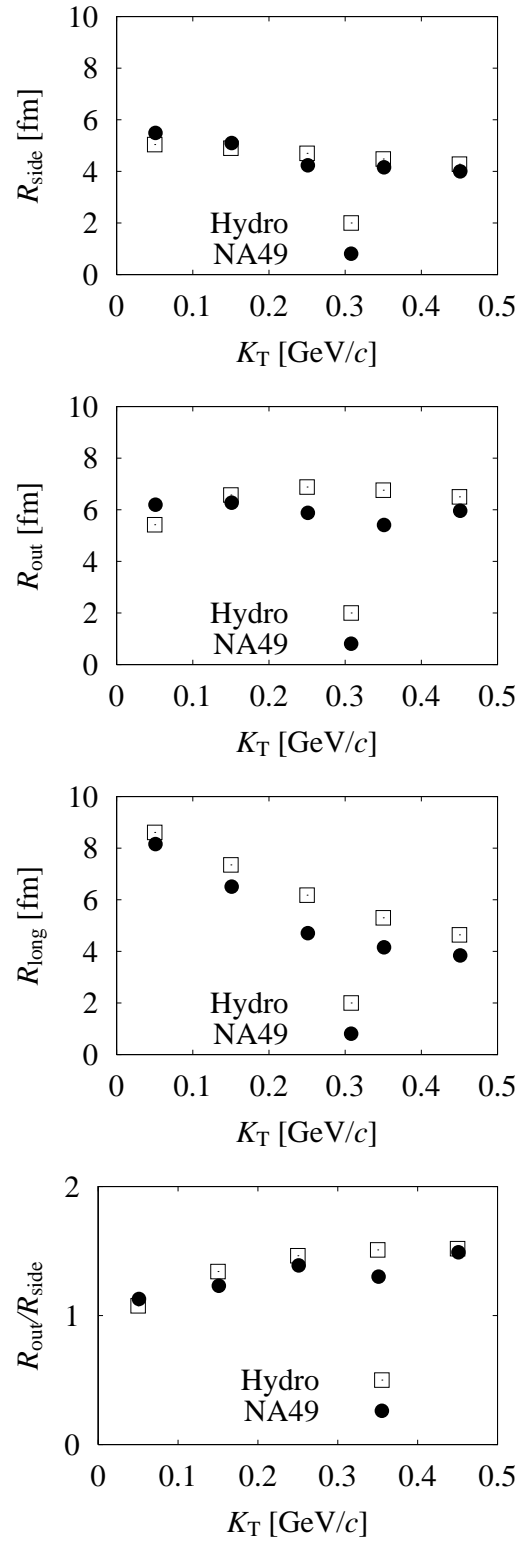


FIG. 19: HBT radii at SPS. From top to bottom, R_{side} , R_{out} , R_{long} and $R_{\text{out}}/R_{\text{side}}$ are plotted. Closed circles denote the experimental data from the NA49 collaboration [40]. Open squares stand for our results. Experimental acceptance is $2.9 \leq Y \leq 3.4$ in the laboratory system.

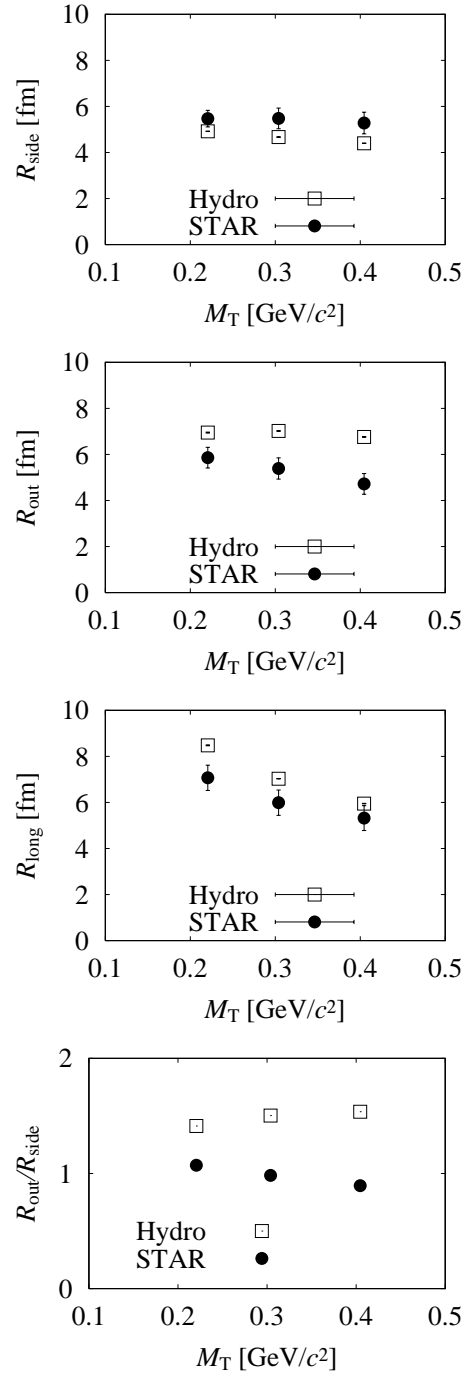


FIG. 20: HBT radii at RHIC. From top to bottom, R_{side} , R_{out} , R_{long} and $R_{\text{out}}/R_{\text{side}}$ are plotted. Closed circles denote the experimental data from the STAR collaboration [41]. Open squares stand for our results. Experimental rapidity acceptance is $|Y| \leq 0.5$. Three data points correspond to $0.125 \leq K_T \leq 0.225$ GeV/c, $0.225 \leq K_T \leq 0.325$ GeV/c and $0.325 \leq K_T \leq 0.45$ GeV/c, respectively.

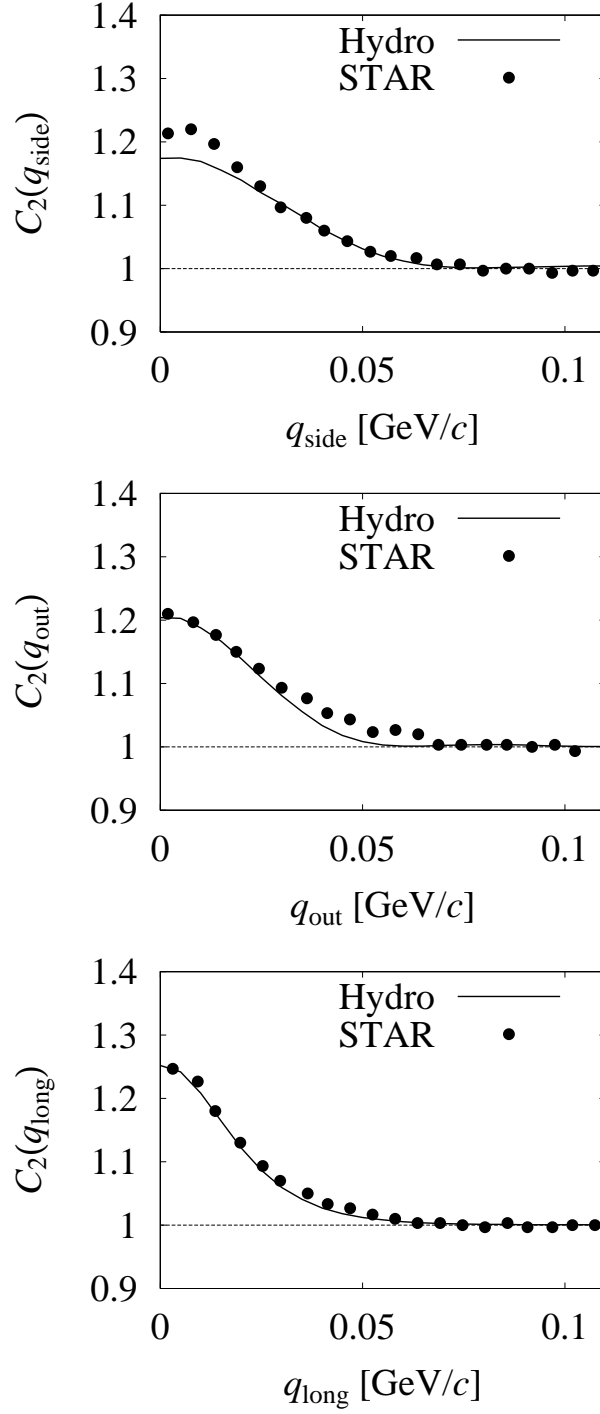


FIG. 21: Correlation functions projected onto each component of relative momenta. From top to bottom, sideward, outward and longitudinal correlation functions are displayed, respectively. Each correlation functions are integrated from 0 to 35 MeV with respect to other two components and corrected by a common λ factor.

Tables

TABLE I: Initial parameter set.

	SPS Pb+Pb	RHIC Au+Au
Maximum initial energy density ϵ_{\max}	5.74 GeV/fm ³	6.0 GeV/fm ³
“Maximum” initial net baryon density n_{B0}	0.7 fm ⁻³	0.125 fm ⁻³
Longitudinal gaussian width σ_{η} of initial energy density	0.61	1.47
Longitudinal extension η_0 of the flat region in the initial energy density	0.48	1.0
Longitudinal gaussian width σ_D of the initial net baryon density	0.52	1.4
Space-time rapidity η_D at maximum of the initial net baryon distribution	0.82	3.0
Gaussian smearing parameter σ_r of the transverse profile	1.0 fm	1.0 fm
Freeze-out condition	$E_f = 70$ MeV/fm ³	$T_f=125$ MeV

TABLE II: Output quantities from the numerical solutions.

	SPS Pb+Pb	RHIC Au+Au
Net baryon number	305	131
Mean freeze-out temperature	123.2 MeV	125.0 MeV
Mean chemical potential at freeze-out $\langle\mu_B\rangle$	281.6 MeV	76.1 MeV
Mean transverse flow velocity $\langle v_T \rangle$ of the fluid at $ \eta < 0.1$	$0.467c$	$0.509c$
Lifetime of the QGP phase τ_{QGP}	2.67 fm/ c	2.92 fm/ c
Lifetime of the mixed phase τ_{MIX}	11.12 fm/ c	12.61 fm/ c
Total lifetime of the fluid τ_{HAD}	17.74 fm/ c	18.94 fm/ c